DOI: ADD DOINUMBER HERE

Numerical framework for aerodynamic and aeroacoustics of bio-inspired UAV blades

Robbie WILKINS and Abdessalem BOUFERROUK*†*
** University of the West of England, BS16 1QY BRISTOL, United Kingdom*
† Corresponding Author: abdessalem.bouferrouk@uwe.ac.uk

Abstract

With the aim to understand and control the noise from small unmanned aerial vehicles (UAVs), this work presents a numerical framework for small-scale rotor blade, employing a bio-inspired finlet design. The simulation framework employs Direct Eddy Simulation (DES) for aerodynamics and Ffowcs-Williams-Hawkings acoustic analogy (FW-H) for acoustic data. Aerodynamic and aero-acoustic validation of the framework for a hovering case is achieved using a baseline DJI-9450 rotor blade, with good agreement shown between experimental and numerical data. An idealized blade model for finlet design, suitable for aeroacoustic studies, is then created and compared against the DJI-9450 baseline model. Although no reliable acoustic data could be obtained with finlet design due to computational limitations, turbulence lifting of smaller-scale eddies is observed for the finlet design, indicating the potential to reduce noise using this technology based on previous findings. Initial finlet design and numerical testing is completed for the purpose of future noise-optimisation studies, where the finlet treatment only causes a negligible effect on the blade aerodynamics.

1. Introduction

The use of UAVs has grown in recent years, with a general strive towards optimisation and efficiency gains leading the front [1-2]. One of the major limiting factors to this 'optimised' future, however, is the noise generated particularly in urban environments, causing significant annoyance to humans. Noting the growing trend of UAV utilisation, and aiming for UAV acceptance within the population, NASA [3] suggested high-level goals to be addressed, where the focus should be towards measured and simulated acoustic data acquisition, for predictive model and optimisation research purposes.

UAV noise, primarily aerofoil self-noise, is generally split into tonal (discrete frequency) noise and broadband (general frequency coverage) noise [4], caused by the interaction of the blade surfaces with the unsteady flow in the form of turbulence. Tonal noise is divided into deterministic components of 'thickness' and 'loading' noise, and 'blade-vortex interaction' (BVI) noise [5]. Broadband noise contains the non-deterministic 'loading' noise components, categorised into 'turbulence-ingestion noise', 'blade-wake interaction' (BWI) noise, and 'blade self-noise' [6]. Numerically predicting these phenomena generally involves decoupling acoustic pressure fluctuations and aerodynamic pressure fluctuations, due to acoustic pressure fluctuations occurring orders of magnitude lower than aerodynamic pressure fluctuations, and numerical methods being incapable of coping with the higher-order accuracy required. Usually, the FW-H analogy is used, derived for walls/ moving bodies enclosed within a permeable or porous source surface [7].
Much attention, both numerically and experimentally, has been paid to optimisation for noise control purposes through passively reducing the unsteady turbulent flow, including serrated-trailing-edge (STE) aerofoil and flat plate designs [8-20], whale-fin-wave inspired blades [21], serrated-leading-edge (SLE's) aerofoil, flat plate, and propeller designs [22-25], with further systems reviewed in [26], including BL tripping systems, porous metal inserts, and/or a combination of all mentioned. Bio-inspired flat plate, aerofoil, rotor, and propeller systems have also recently become a popular solution [27-29]. Bio-inspired designs have demonstrated significant noise-reductions over conventional design both numerically and experimentally and they are being considered as viable noise reduction technologies.

Upstream surface treatments, such as 'finlets' have demonstrated significant reductions in aerofoil and flat plate TE noise [30-33, 36-37] and will be studied in this paper. The reduced noise is attributed to turbulent kinetic energy 'channelling' and 'lifting' away from the TE for the smaller-scale eddies, leading to a reduced edge scattering, and lowered power spectral density (PSD) for the low-mid or mid-high frequencies in the TE region. While previous work [36-37] presented the effectiveness of upstream surface treatments on the NACA0012 aerofoil, and further works upon finlet 'rails' and 'fences' [34-35, 38-39] have been conducted for flat plate and aerofoil uses, application of this to the field of rotors for UAV or propeller use has not been explored. In the present work, the finlet design is considered and

DOI: ADD DOINUMBER HERE

applied to an idealized DJI-9450 blade profile, with aerodynamic and aeroacoustics comparisons drawn, and initial finlet blade design results presented.

2. Methodology

2.1 UAV Case Definition

A drone is chosen for the work based upon three goals: to provide a baseline for numerical validation; to allow for further design-optimisation, and to be commercially available. The DJI-Phantom 3 and DJI-9450 rotor form the baseline for the current work. Figure 1 displays the single drone rotor that is modelled. GrabCAD was used to obtain the rotor geometry in .STEP file format [40]. The chosen UAV definition and operating conditions are presented in table 1 (based on general drone use and holding numerous validation data sets), while table 2 lists blade dimensions.

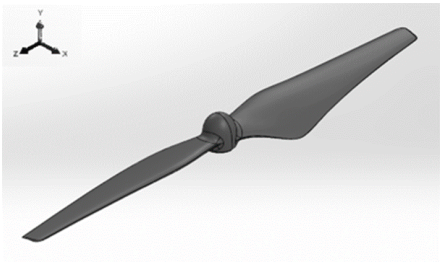

Figure 1- DJI-9450 single- rotor configuration CAD

Table 1- UAV Case Definition & Operating Conditions

Parameter	Choice	Unit
Drone	DJI-Phantom 3/Phantom 3 Pro	n/a
Rotor	DJI-9450	n/a
RPM	6000	Degrees or Radians
Operation phase	Hovering	n/a
Operating conditions	Sea level	n/a

Table 2- DJI-9450 rotor dimensions

Parameter	Nomenclature	Dimension [m]
Average Chord	C_{avg}	0 025
Rotor diameter	D	0 239
Rotor tip-chord	C_{tip}	0 01
Rotor minimum tip-clearance	min_{tip}	~0 167 (~0 7D)

2.2 Computational Set-up

Following the numerical work in [41], identical computational domain and corresponding BCs are chosen. Figure 2 shows the current computational domain employing similar dimensions to that in [41]. The 'bullet-shaped' domain spans a radius of $10 \times L$ in the rotor-plane, $5 \times L$ in the upstream spherical extent, and $20 \times L$ downstream of the rotor-plane. Within this *static* extent, a $1\ 1 \times L$ diameter cylindrical *rotating* domain encapsulates the rotor, with $0\ 2 \times L$ above and below the upper- and lower-rotor surface limits. The BC's chosen simulate hovering, with an outlet directly downstream of the rotor-plane, in the direction of the jet-stream, and inlets surrounding all-but the outlet, where no jet-stream would occur. Following [41], the $k - \omega\ SST$ turbulence model is utilised by default in the work- unless stated overwise. To accurately model the boundary layer, 20 prism-layers discretized a $0\ 001m$ height over the rotor surface, corresponding to a wall-normal viscous unit resolution of $y+< 5$, for all simulations. Outside of the prism-layer region, the rotational- and static-domain grid-sizing is altered, based upon the desired resolution during mesh independence studies. The solution procedure followed an initialization through steady conditions, employing the 'moving reference

DOI: ADD DOINUMBER HERE

frame' model for the rotational domain, with a 'sliding mesh zone' later utilised for the rotational domain of the transient solution.

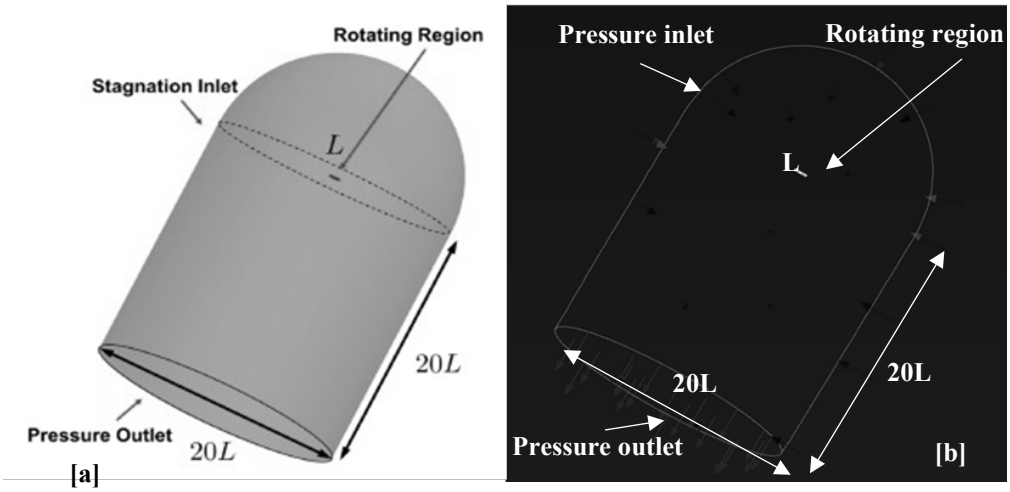

Figure 2- Computational domain of [41] (a), and the present computational domain (b)

The procedure is suggested in [42] to reduce the computational time of a case with zone translational- or rotational-velocities. For solution stability, the steady and unsteady solutions used differing methods and controls, as suggested by [42], and listed for steady and transient solvers in table 3. If the method, control, or relaxation is not mentioned, the default within ANSYS Fluent is employed. Governing equation and averaged C_T residual convergence is set to >1e-5 for steady-state, and unsteady-state, however for each individual timestep, as opposed to the whole solution, with a maximum of 20 iterations per timestep completed. In line with [41], table 5 lists the unsteady time settings used within the present work. The timestep size corresponds to 3° rotation per timestep, or 120 timesteps per rotation. Therefore, 0 01s of physical time pass per rotation, or a rotational frequency of 100Hz, and incompressible Reynolds number of 1.25e+5. For the flow-field, 3600 timesteps, or 0 3s is run for- unless stated otherwise.

Table 3- Steady-state and transient solver settings, controls, & relaxations

Criteria	Steady state	Transient run
Pressure-velocity formulation	SIMPLE	Coupled
Velocity scheme	2nd Order	2nd Order
Pressure scheme	PRESTO!	2nd Order
Momentum under-relaxation	0 5	0 7
Pressure under-relaxation	0 7	0 7

Table 4- Default transient time-settings

Criteria	Nomenclature	Selection	Unit
Timestep size	Δt	8 33e-5	Seconds
Timesteps per rotation	$\Delta t/rot$	120	n/a
Timesteps	n/a	3600	n/a
1-rotation physical time	n/a	0 01	Seconds
Rotational frequency	f_{rot}	100	Hertz
Reynolds number	$Re_{v_{tip}c_{avg}}$	1 25e+5	n/a

Acoustic modelling and related parameters chosen for the present work are inspired by previous works on similar case [41,43-44], listed in table 6. Once acoustic source data is acquired, the unfiltered signal is processed through Fast Fourier Transform (FFT), with a Hamming window applied.

Table 5- Default acoustic settings & quantities

Criteria	Nomenclature	Selection	Unit
Flow periods	n/a	0-30	n/a
Source-data periods	n/a	30-50	n/a

DOI: ADD DOINUMBER HERE

Reference pressure	atm	1	Atmosphere
Reference sound pressure	Pa	2e-5	Pascal
Speed of sound	a	340	Meters/second

3. Model Validation

3.1 Grid independence

The focus of grid refinements is the rotational domain, to quantitatively capture rotor-induced-thrust, through discretizing the CAD geometry. Quantitatively, capturing flow features is as essential to observe rotor wake interaction, and how this affects blade loading, and wake-vortex interactions, and thus acoustic wave propagation and attenuation. To capture this, a wake-zone is discretized immediately downstream of the rotational domain, containing ~1 000 000 elements, with the rotor at the centre of the $0\ 625 \times L$ radius cylinder, and a downstream distance from the rotor of $2\ 5 \times L$. The base grid is depicted in figure 3. To judge quantitative grid convergence, the thrust coefficient 'C_T' is measured (Equation 1), with averaged values across the final three rotations being taken, corresponding to 0 03s in flow time, while flow features are observed for the qualitative investigation.

$$C_T = \frac{T}{\rho A(\Omega R)^2} \tag{1}$$

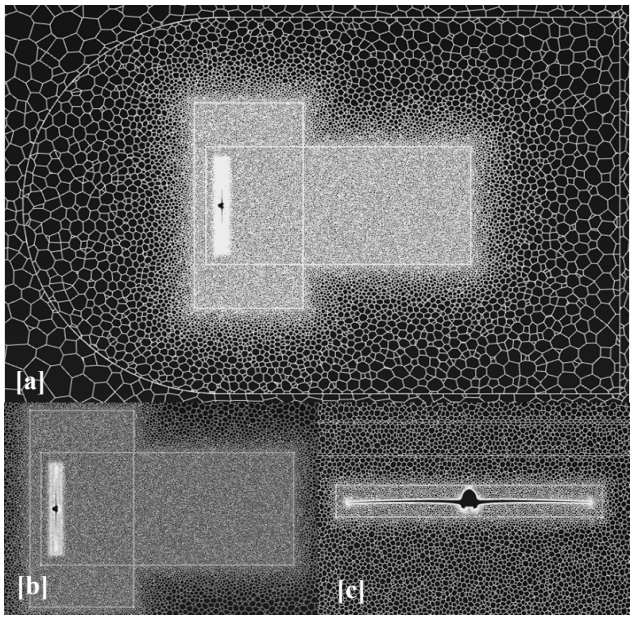

Figure 3- Base single-rotor grid with the far-field (a), near-field (b), and rotational domain (c) depicted.

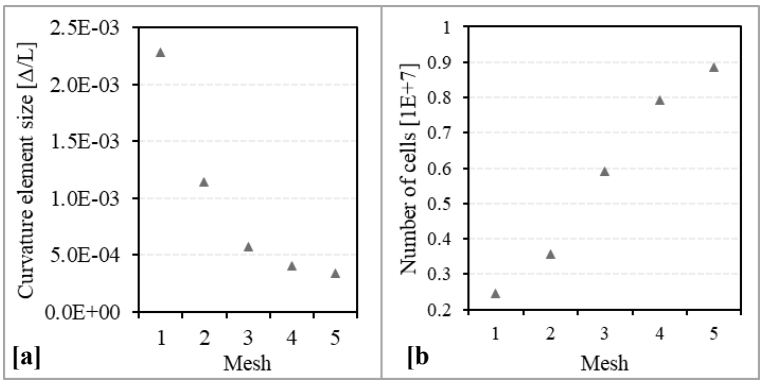

Figure 4- Curvature sizing-function study with normalized sizing's (a), and resulting cell-counts (b)

DOI: ADD DOINUMBER HERE

To accurately capture and discretize the blade curvature for capturing the high-gradient flow physics about the LE and TE of the blade, the blade face-curvature function is altered. figure 4 (a) displays the sizing's applied, normalized by L, and figure 4 (b) provides the resulting number of cells, with figure 5 depicting comparison results, figure 6 displaying the resulting grids for the coarse, medium, and fine meshes (meshes 1, 3, and 5), with grid independence achieved by mesh 3, with mesh 5 deviating only ~0 12% from this, for an additional ~49 5% increase in grid elements. In terms of model validation, mesh 3 deviates only ~10 4% from the experimental measurement of [45]. Mesh 3's data point is highlighted (darker), within figure 5.

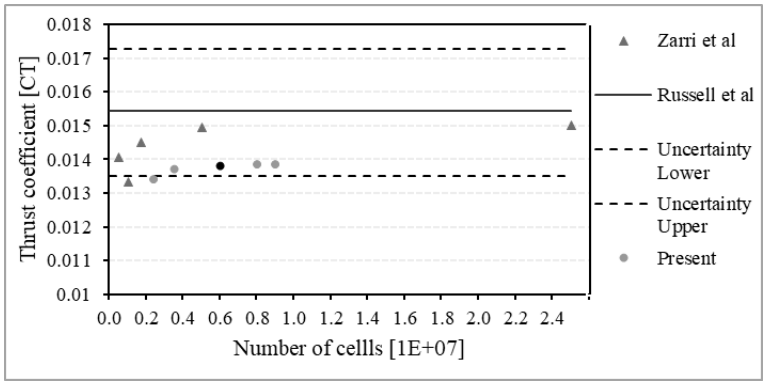

Figure 5- Comparison results of curvature sizing-function study

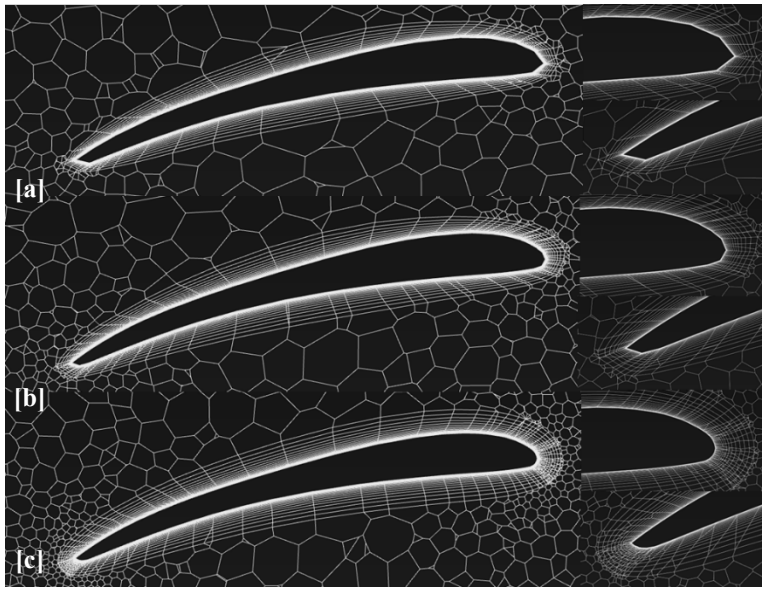

Figure 6- Resulting coarse (a), medium (b), and fine (c) meshes for curvature-function study

3.2 Turbulence Effects

To capture smaller-scale flow features for acoustic surface pressures, DES is compared with $k-\omega\ SST$. Figure 8 displays the time-history of instantaneous thrust produced by the blade, over 0 01s flowtime, or 1 rotation, with data from the 30th rotation at 0 3s flowtime. Observing figure 7, DES results have an oscillation of amplitude ~0 $004N$, with this oscillation pattern shifting upwards towards the second half of the period. The $k-\omega\ SST$ experiences an ~0 $001N$ oscillation amplitude, that is shifting downwards slightly towards the end of the period. Figure 8 displays the averaging of $k-\omega\ SST$ from the larger force fluctuations present within DES, presumably due to the improved scale- resolving of DES. An interesting point is the smaller sub- oscillations present in the $k-\omega\ SST$ time- history, possibly due to the model being limited at the order of modelling below 1e-4 resolution and leading to solver instability.

DOI: ADD DOINUMBER HERE

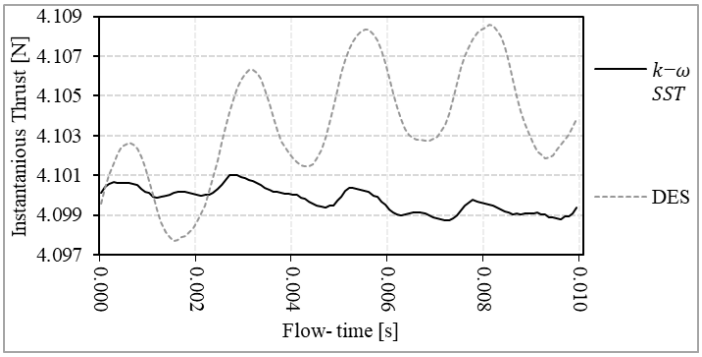

Figure 7- Single-rotor turbulence model comparison results of thrust time-history, over 0 01s flow-time

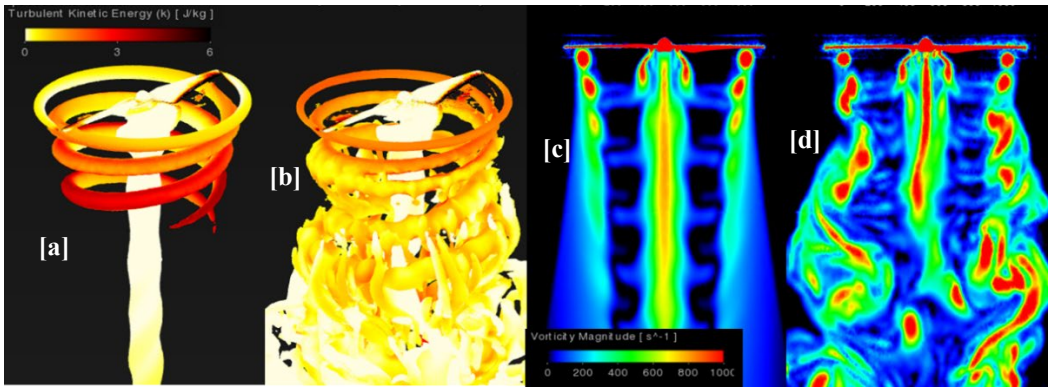

Figure 8- $k-\omega$ SST (a), and DES (b) raw Q-criterion iso-surface contours, filtered at $35000s^{-1}$, painted with TKE contours at 0 3s flowtime, and $-\omega$ SST (c), and DES (d) vorticity magnitude contours at 0 3s flowtime.

Figure 8 (a & b) displays raw Q-criterion iso-surface contours, filtered at $35000s^{-1}$, painted with TKE, for $k-\omega$ SST and DES cases, respectively. Clearly, both figure 8 (a & b) capture the core-wake, in addition to the tip-vortices. The deviation occurs past the approximately third downstream tip-vortex, where figure 8 (a) diffuses off, whereas figure 8 (b) moves into tip-vortex breakdown and core-wake interactions. Figure 8 (c & d) better displays this, with tip-vortex diffusion occurring by the 3rd eddy in figure 8 (c) but continuing downstream in figure 8 (d). The comparison depicts the clarity of DES in flow-field prediction, while quantitatively both models provide similar averaged values.

3.3 Aero-acoustic Validation

3.3.1 Definition

To validate the acoustic prediction capacity of ANSYS Fluent, and the current case, the acoustic setup numerically implemented by [41] is employed. Experimental [45], and Lattice-Boltzmann numerical results [46], of the same case, are also compared. The rotor observer locations employed in [41], translated into ANSYS Fluent, are listed with their coordinates in table 7, where they form an arc of 7 97 × D (1 905m radius from the blade origin).

Table 6- Present observer location coordinates [m]

Observer	x-axis	y-axis (rotational axis)	z-axis
45°	0	1 347	1 347
67.5°	0	0 729	1 760
90°	0	0	1 905
112.5°	0	-0 729	1 760
135°	0	-1 347	1 347

Sound pressure level (SPL) L_p in dB (Equation 2), is measured to quantitatively judge the acoustic validation. To qualitatively judge the sources, dominant harmonic frequencies are identified; in the case of rotating objects, the Blade Passing Frequencies (BPF's), defined in Equation 3, is compared. The first five BPFs for this case correspond to the frequencies of 200, 400, 600, 800, and 1,000 Hz. In Equation 2, p'_{rms} is the root mean square (rms) of acoustic pressure

DOI: ADD DOINUMBER HERE

fluctuations [Pa] and is the reference pressure (20 μPa). In Equation 3, B is the number of blades, n is the BPF number and Ω is the rotation frequency $[rad/s]$.

$$f_{BPF} = B \times n \times \frac{\Omega}{2\pi} \quad \textbf{(2)}$$

3.3.2 Source selection

To choose the optimal source surface for acoustic far-field predictions, an 'open' near-field surface and the rotational domain surface are compared- both act as permeable surfaces, treating the interior rotor source as a quadrupole source [47]. A permeable source is used rather than the blade wall itself due to the noise generation being exterior to the wall surface [47], in addition to capturing the vortical-structure generated noise. This approach is tested and utilised within previous literature [44, 48] based upon the recommendations of [49] who explore the FW-H surface selection in detail. It was found (not shown) that the inner 'open' and rotational source surfaces both capture the first five BPFs based on SPL trends, despite some reduction in SPL for the inner 'open' source beyond BPF of 2.

Comparing extracted BPF SPL values to the literature, figure 9 (a) presents BPF 1 values for all observer locations, while figure 9 (b) presents BPF 2 values. Figure 9 (a) shows almost identical values for both surfaces, where the trend achieved by the literature is followed. Averaging the five observer location SPL values, figure 10 (a) presents deviation from the experimental data [45], where ~15 0% & ~15 3% deviation yielded for the rotational and inner 'open' surfaces, respectively. This appears like Zarri et al's [41] deviation, though ~10 0% greater than Thurman et al's [46]. Observing figure 10 (b) however, the inner 'open' source does not follow the trend for the 45° observer, leading to an ~34 0% deviation from Russell et al's [45] data, depicted in figure 10 (b). Observing the rotational source in figure 9 (b), the trend is followed, and corresponding figure 10 (b) deviation is only ~11 0% from Russell et al's [45] data - like [41, 46]. Improved accuracy from the rotational source was further evidenced when investigating SPL trends for BPF 1-5 for observers 90° & 135°. Rotational source SPL is closer to the experimental data for both locations, with averaged deviation across all BPF's of only ~8% & ~18 0%, for 90° & 135°, respectively. The inner 'open' source, however, exhibits a ~32 0% & ~42 0% deviation from experimental data for 90° & 135°, respectively.

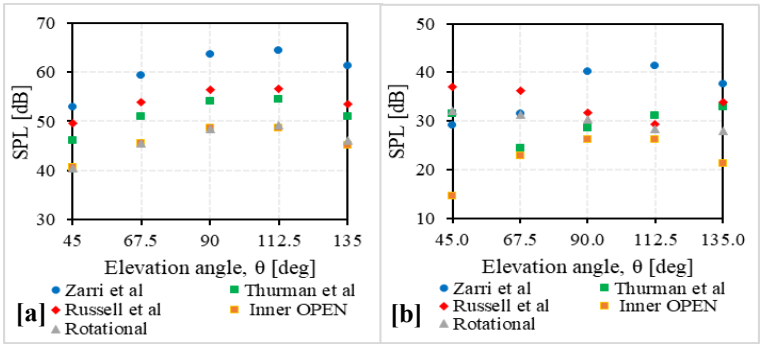

Figure 9- Comparison of SPL against elevation angle for BPF 1 (a) & BPF 2 (b) of the rotational and inner 'open' FW-H volume-source-surface contributions.

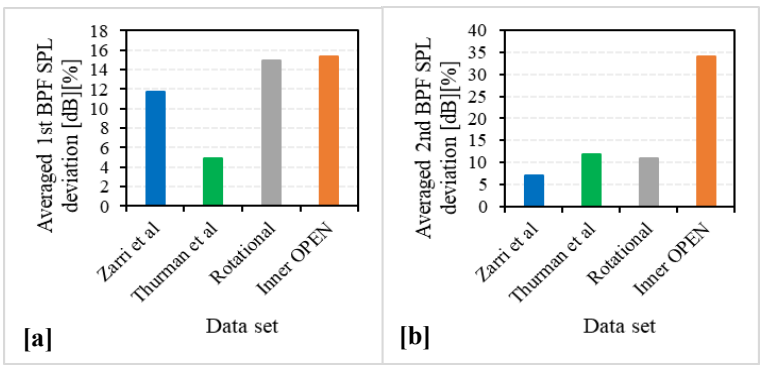

Figure 10- Comparison of averaged SPL deviation from Russell et al. (2016) experimental data for BPF1 (a) & BPF2 (b) of the rotational and inner 'open' FW-H volume-source-surface contributions.

DOI: ADD DOINUMBER HERE

3.3.3 Temporal Resolution

In terms of achieving accurate temporal resolution, Equation 3 formulates the acoustic Courant Number (CFL), a function of the spatial and temporal CFLs. Achieving a CFL equal to unity implies harmony between spatial and temporal resolution. Table 9 lists the timesteps of interest, with corresponding timestep and CFL details also listed.

$$CFL_{accoustic} = \frac{CFL_{spatial}}{CFL_{temporal}} = \frac{a_0 \times \Delta t}{\Delta x} \quad (3)$$

In Equation 4, a_0 is the speed of sound, Δt is the timestep and Δx is the cell size.

Table 7- Temporal-resolution timesteps & details

Δt [s]	$°rot/\Delta t$	$\Delta t's$ $/1rot$	Flow-$\Delta t's$	Acoustic-source-$\Delta t's$	$CFL_{accoustic}$	f_{max} [Hz]
8 33e-5	3	120	3600	2400	~16	6000
1 39e-4	5	72	2160	1440	~27	3600

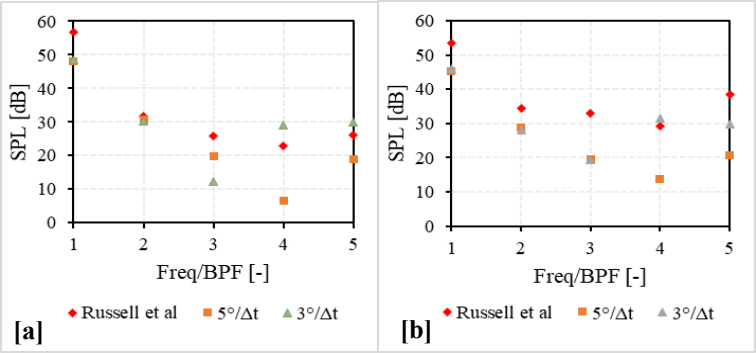

Figure 11- Comparison of SPL against BPF1-5 for 90° (a) & 135° (b) for 5°/Δt & 3°/Δt against experimental data.

Figure 11 (a & b) show a clear trend of almost exact BPF SPL values for BPF 1 & 2, then a deviation where 3°/Δt SPL tends towards the data [45], whereas 5°/Δt tends away. Interestingly, 5°/Δt SPL data conforms more to the shape-trend of Russell et al's [45] data. Finally, table 10 lists deviation from the data [45], proving improved prediction accuracy with 3°/Δt, as is expected from the closer-to-unity $CFL_{accoustic}$.

Table 8- Temporal-resolution BPF 1-5 averaged SPL deviation [dB][%] from Russell et al's [45] data

Δt [s]	90° observer	135° observer
3°/Δt	~~8 1%	~17 9%
5°/Δt	~24 1%	~32 0%

4. Finlet design

4.1 Design philosophy

Finlet design philosophy is often based upon the designs introduced by Clark et al. [30] for the DU96-W-180 blade aerofoil. Figure 12 displays the baseline designs through idealized versions of Clark et al. [30] work, with CAD produced by Boding & Sharma [34]. The finlet design is proving increasingly popular over the rail design, seemingly due to the inherent structural advantage of the finlet compared to rail design, as both were reported to heavily influence surface pressure spectra with noise attenuations up to 30dB [30].

DOI: ADD DOINUMBER HERE

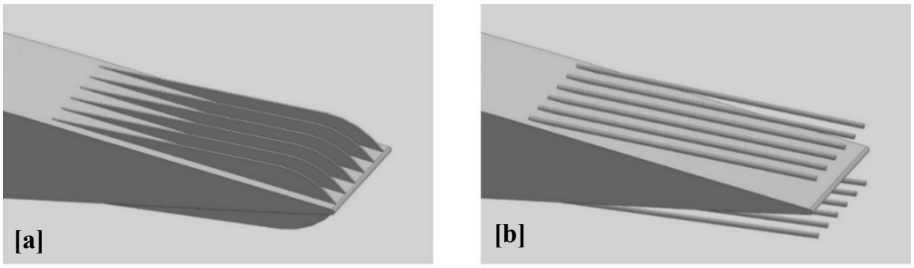

Figure 12- Idealized finlet fence (a), and rail (b) designs, inspired by [30], with CAD produced by [34].

4.1.1 Finlet profile design

The finlet profile from the LE until the maximum height, h_f, is designed based upon a turbulent boundary layer shape, as introduced in [30], leading to the relation of Equation 4, where a constant, α, is introduced in [36] to alter the LE profile equation, with α equating to a value leading to h_f being reached at half the finlet length, l_f. Generally, the TE of the finlet design is curved to ease destructive pressure gradients produced in the region when interacting with the TE flow- an example being a TE radius equivalent to h_f, as used in [36-37]. Defining essential finlet design parameters, figure 13 displays and label the NACA0012 aerofoil case with finlet treatments produced by [36].

$$y_f \equiv \alpha \times x_f^{4/5} \tag{4}$$

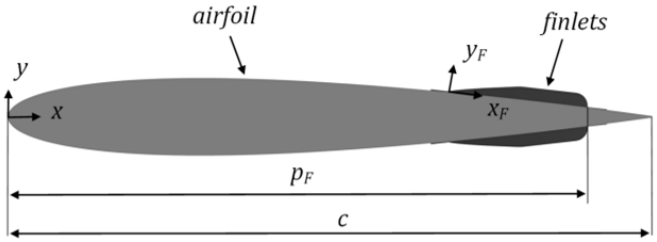

Figure 13- 2-D finlet design schematic applied to a NACA0012 aerofoil [36].

The finlet design parameters are: chord (c), spacing (s_f), thickness (t_f), local length (x_f), local thickness (y_f), maximum length (l_f), maximum height (h_f), and end position (p_f).

4.2 Case definition

The current state-of-the-art of finlet design, as discussed in [30-39] relates to aerofoil and/or flat plate studies. For the present work, sizing inspiration from the works is applied to the DJI-9450 rotor case. Table 12 summarises the design choices based upon the local blade chord, c_{local}, with justification of each parameter.

Table 9- Present finlet design choices

Parameter	Values (m)		Justification
c_{local}	**At $0.5 \times r/R$**	**At r/R**	Surface treatment applied only from $0\,5 \times r/R$ to r/R as predominantly where blade TE-wake reacts.
	0 0227	0 0106	
Re_x	$5\,70 \times 10^4$	$5\,33 \times 10^4$	Calculated for turbulent BL.
s_f	0 002, 0 004, 0 006		Observed to be independent of the chord-based Reynolds number in range of $2\,5 \times 10^6 \leq Re_x \leq 3 \times 10^6$ [32-33] and $3\,87 \times 10^5 \leq Re_x \leq 7\,7 \times 10^5$ [30-31].
t_f	0 0000417		Scaled to blade average chord, c_{avg}, through equation 5 and 6 for t_f and l_f respectively.
l_f	0 00493	0 00231	
h_f	0 000780	0 000370	$h_f/\delta^{99} = 0\,5\ to\ 0\,8$ relation recommended [30-33].

DOI: ADD DOINUMBER HERE

p_f	$0.9c_{local}$	Finlet position observed to generally be most efficient.

$$t_f = c_{avg} \times \frac{t_{f_{ref}}}{c_{ref}} \quad (5)$$

$$l_f = c_{avg} \times \frac{l_{f_{ref}}}{c_{ref}} \quad (6)$$

4.3 CAD geometry

Prior to implementing the parameters for the finlet design, the base GrabCAD [40] geometry was evaluated to be too complicated to implement finlets onto in a linearly changing fashion from 0 5 $\times r/R$ to r/R, due to the blade morphing its twist and chord in a non-linear fashion. To simplify the CAD model, a linearly morphing relationship was implemented, with the resulting CAD in figure 14 (a & b). It is worth noting that this CAD is before fillets have been applied to each model to simply show the blade.

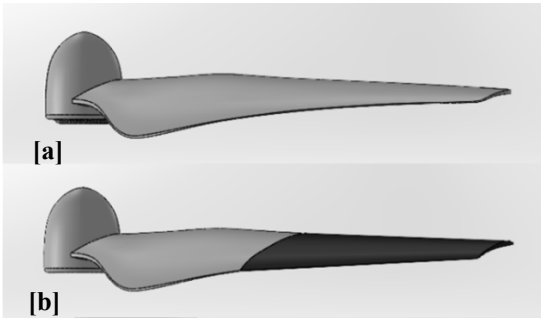

Figure 14- Present DJI-9450 GrabCAD blade [40](a) and idealized CAD (b).

Implementing the design choices (table 12) onto the idealized blade (figure 14) results in the geometry of figure 15, displaying the geometry utilising an s_f of 0 004m. Figure 15 (a) displays the entire blade with finlets highlighted darker, figure 15 (b) shows the side-view of this, while figure 15 (c, d, & e) highlights the finlet profiles, with figure 15 (d) located at $r/R =$ 0 5, and figure 15 (e) at $r/R =$ ~0 97.

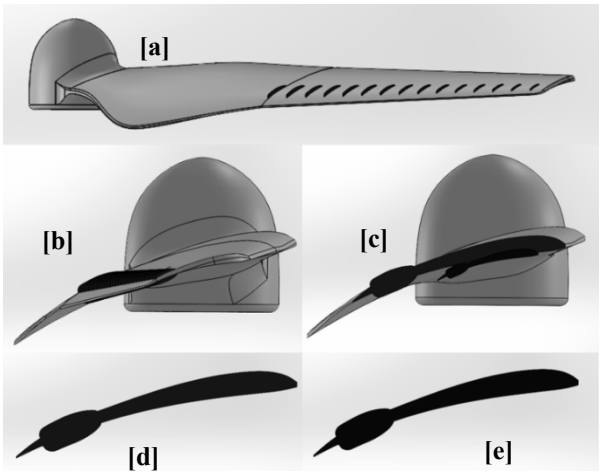

Figure 15- Present finlet blade geometry depicting blade iso-view (a), side-view (b), & finlet profiles (c), with 0 5 $\times r/R$ (d) & ~0 97 $\times r/R$ (e).

5. Results

5.1 Idealized model

To validate the idealized model prior to studying the finlet effects, aerodynamic and aeroacoustics comparisons are drawn against the GrabCAD model [40]. To fairly compare, spatial and temporal resolutions, settings and models were used as those in section 3.

DOI: ADD DOINUMBER HERE

The resulting idealized blade grid is almost identical to that of the GrabCAD [40] blade profile, at $0\ 5 \times r/R$, and so is not presented. Mesh metrics are listed in table 13, showing similar quality is achieved through the mesh translation from the GrabCAD [40] onto the idealized model.

Table 10- Idealized mesh translation comparison

Metric	Idealized	GrabCAD [40]
Elements	6254289	4619756
Nodes	21043019	18268241
Maximum aspect ratio	694 38	732 64
Minimum orthogonal quality	0 029	0 0392

Comparing the idealized blade aerodynamics to the GrabCAD [40] model, table 14 lists period averaged C_T values for the 30th rotation, at 0 03s flowtime, yielding an ~32.6% deviation between the two blades. This deviation is quite large, however is expected due to the differing blade geometries past $0\ 5 \times r/R$. Further comparison is shown through pressure coefficient (C_p) plots at $r/R \times \in 0\ 667, 0\ 833, 0\ 99$ depicting the greater surface area of the idealized blade the further away from $0\ 5 \times r/R$, presumably leading to the deviation mentioned. The main point about Figure 16 is the similarity in general trends.

Table 11- Idealized blade aerodynamic comparison

	GrabCAD	Idealized	Deviation [%]
Period averaged C_T	0 0132	0 0176	32 6

5.2 Finlet model

Finlet results employed the exact case as section 3, as in section 5.1.
The resulting finlet-blade mesh is observed and compared in figure 17 to the idealized model profile, at $0\ 5 \times r/R$. Mesh metrics are listed in table 15, showing the base-finlet blade, with $0\ 004m\ s_f$, achieves similar quality through the mesh translation. The sizing applied yields an average discretization of 55 cells along the finlet edge, with a maximum of 74, and minimum of 36.

Table 12- Finlet mesh translation comparison

Metric	$\mathbf{0\ 004\ s_f\ [m]}$	Idealized
Elements	7736909	6254289
Nodes	23385702	21043019
Maximum aspect ratio	606 70	694 38
Minimum orthogonal quality	0 009	0 029

Comparing the finlet blade aerodynamics to the idealized model, table 16 lists period averaged C_T values for the 30th rotation, at 0 03s flowtime, yielding an ~0 5% deviation between the two blades. This deviation proves almost negligible, proving the 0 004 s_f finlet blade maintains its aerodynamic performance. Further comparison through pressure coefficient (C_p) plots is not presented due to almost negligible difference between the idealized and 0 004 s_f values at $r/R \times \in 0\ 667, 0\ 833, 0\ 99$.
Observing effects to the flow-field, specifically paying attention to the region post-finlets, where unsteady surface pressure fluctuations play their part in noise generation, it is observed that the displacing of smaller-scale eddies, through the TKE fluctuations observable in figure 18 (b) within the white box, as opposed to figure 18 (a) is apparent. Figure 18 (c & d) further evidences this, where smaller-scale fluctuations are 'lifted' above the finlet upper surfaces in figure 18 (b) as highlighted within the white box, as opposed to the larger-scale turbulence evident above the same area in figure 18 (a). Future work will improv resolution in this region to better display the differences.

Table 13- Finlet blade aerodynamic comparison

	Idealized	$\mathbf{0\ 004\ s_f}$	Deviation [%]
Period averaged C_T	0 0176	0.0175	~0 5

DOI: ADD DOINUMBER HERE

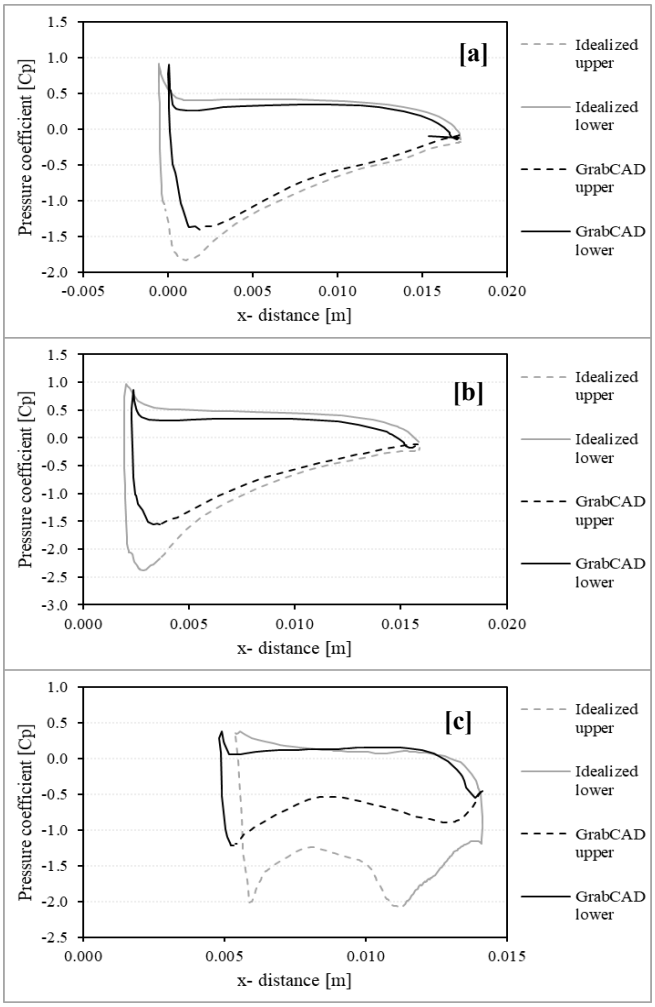

Figure 16- Pressure coefficient plots comparing Idealized and GrabCAD [40] blade profiles at $r/R \times \in 0\ 667(a), 0\ 833(b), 0\ 99(c)$.

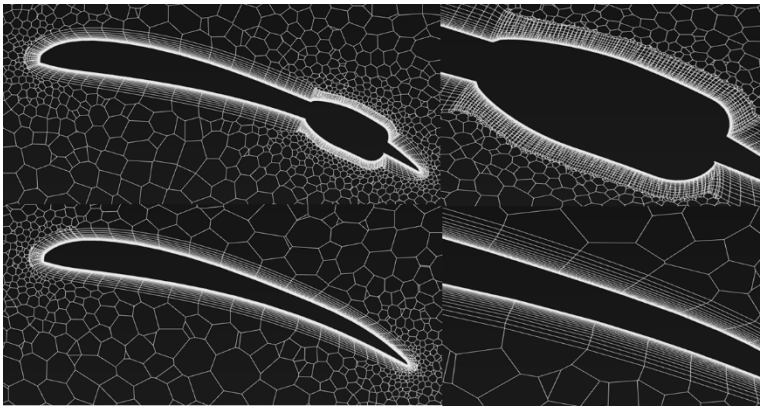

Figure 17- Profile-view at $0.5 \times r/R$ *for the finlet (a) and idealized (b) grids.*

DOI: ADD DOINUMBER HERE

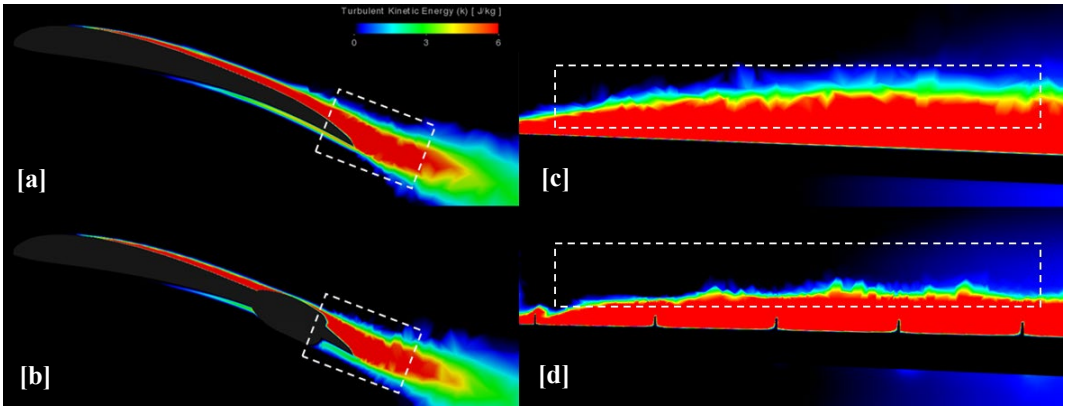

Figure 18- Comparison of idealized and finlet flow, at 0 5 ×r/R (a & b, respectively), through TKE contours, and at 0 95 ×c, across 0 95>r/R>0 5 (c & d, respectively)

Conclusions

Aerodynamic and aero-acoustic numerical validation and analysis of the DJI-9450 blade has been conducted to provide a numerical framework for finlet blade design. The numerical analysis uses ANSYS Fluent for both flow and aeroacoustic predictions. The simulation framework employs Direct Eddy Simulation (DES) for aerodynamics and Ffowcs-Williams-Hawkings acoustic analogy (FW-H) for acoustic data. Initial finlet design and numerical testing of a finlet blade model was completed for future noise-optimisation studies, where a negligible aerodynamic effect of applying the treatments was shown. The averaged CT from CFD deviated by ~11 0% compared with experimental data. Good agreement was also shown between the present CFD and experiments for SPL values, with the rotational source chosen over the tested inner 'open' source, for improved accuracy, deviating ~15 0%, & ~10 9%, for BPF 1 & 2, respectively. Further analysis on BPF 1-5 for observer locations 90° & 135° revealed an averaged SPL deviation of ~8 2%, & ~18 0% for the rotational source, for the respective observer locations. The idealized model for finlet application was shown to deviate ~32 6% from the GrabCAD model for C_T, as expected due to its differing blade geometries past 0 5 $\times r/R$, where C_P plots validated this, displaying greater surface area of the idealized blade past this, presumably adding to the lifting surface and thus the blade's C_T. The effects of finlets on the aerodynamics were shown to be negligible, with an ~0 5% deviation between the idealized model, and the 0 004 s_f finlet blade. Turbulence 'lifting' of smaller-scale eddies, known to be the source of noise reduction for surfaces with finlets, was exhibited with the finlet-blade design. With negligible effects on aerodynamics and turbulence lifting occurring with finlet design, this technology demonstrates its potential for noise reduction on UAV blades. The framework provides a tool for noise-optimisation studies of finlet designs.

Recommendations For Future Work

To improve current simulation results, a few research directions can be explored. Focus should be on reducing the order of near-field mesh resolution to reduce pressure fluctuation diffusion into near-field mesh, for acoustic source-surface purposes to test FW-H surface contributions more fairly. In addition, it is important to understand which surface is most effective at capturing the noise source, adding to existing work on surface selection [49]. Future focus should also be on capturing smaller-scale finlet indued flow phenomena and evaluating their effects more thoroughly. More work is needed to complete the aero-acoustic analysis and comparison of the finlet blade, with a shift then to conducting in-depth aerodynamic and aero-acoustic analysis of the different finlet geometric parameters to observe their effects. Additionally, applying these future works to multi-rotor configurations, looking into the interactional effects when finlets are applied, say, to a quadcopter UAV with two bladed rotors.

References

[1] R. Merkert and J. Bushell, "Managing the drone revolution: A systematic literature review into the current use of airborne drones and future strategic directions for their effective control," J Air Transp Manag, vol. 89, p. 101929, 2020, doi: https://doi.org/10.1016/j.jairtraman.2020.101929.

[2] J. M. Robinson, P. A. Harrison, S. Mavoa, and M. F. Breed, "Existing and emerging uses of drones in restoration ecology," Methods Ecol Evol, vol. 13, no. 9, pp. 1899–1911, Sep. 2022, doi: https://doi.org/10.1111/2041-210X.13912.

[3] NASA Langley Research Centre, "Turbulence Modeling Resource- 2DN00: 2D NACA 0012 Airfoil Validation Case.," Aug. 28, 2020. https://turbmodels.larc.nasa.gov/naca0012_val.html

DOI: ADD DOINUMBER HERE

[4] A. N. Kusyumov, S. A. Mikhailov, L. I. Garipova, A. S. Batrakov, and G. Barakos, "Prediction of helicopter rotor noise in hover," EFM14 – Experimental Fluid Mechanics 2014, vol. 92, no. 02042, pp. 0–5, 2015.
[5] A. F. Deming, "Noise from propellers with symmetrical sections at zero blade angle, II," Dec. 1938. Accessed: Dec. 01, 2022. [Online]. Available: https://ntrs.nasa.gov/citations/19930081438
[6] K. S. Brentner and F. Farassat, "Modeling aerodynamically generated sound of helicopter rotors," Progress in Aerospace Sciences, vol. 39, no. 2, pp. 83–120, 2003, doi: https://doi.org/10.1016/S0376-0421(02)00068-4.
[7] ANSYS, "Chapter 11: Aerodynamically Generated Noise," in ANSYS Fluent Theory Guide , 2022, pp. 407–422.
[8] E. Pang, A. Cambray, D. Rezgui, M. Azarpeyvand, and S. showkat ali, Investigation Towards a Better Understanding of Noise Generation from UAV Propellers. 2018. doi: 10.2514/6.2018-3450.
[9] J. Nixon and S. Dance, "The Sound of the Drone Uprising – Aeroacoustics of Drone Blades," in Quiet Drones. Paris 17 - 21 Oct 2020, Paris, 2020, pp. 1–8. Accessed: Nov. 17, 2022. [Online]. Available: https://openresearch.lsbu.ac.uk/item/8v1w5
[10] T. Chong and A. Vathylakis, "On the aeroacoustic and flow structures developed on a flat plate with a serrated sawtooth trailing edge," J Sound Vib, vol. 354, pp. 65–90, Oct. 2015, doi: 10.1016/j.jsv.2015.05.019.
[11] F. Avallone, W. C. P. van der Velden, D. Ragni, and D. Casalino, "Noise reduction mechanisms of sawtooth and combed-sawtooth trailing-edge serrations," J Fluid Mech, vol. 848, pp. 560–591, 2018, doi: DOI: 10.1017/jfm.2018.377.
[12] S. K. Singh and S. Narayanan, "Control of airfoil broadband noise through non-uniform sinusoidal trailing-edge serrations," Physics of Fluids, vol. 35, no. 2, p. 025139, Feb. 2023, doi: 10.1063/5.0133556.
[13] Z. Ning and H. Hu, An Experimental Study on the Aerodynamics and Aeroacoustic Characteristics of Small Propellers. 2017. doi: 10.2514/6.2016-1785.
[14] N. Intravartolo, T. C. Sorrells, N. Ashkharian, and R. Kim, "Attenuation of Vortex Noise Generated by UAV Propellers at Low Reynolds Numbers," 2017. Accessed: Feb. 16, 2023. [Online]. Available: https://www.semanticscholar.org/paper/Attenuation-of-Vortex-Noise-Generated-by-UAV-at-Low-Intravartolo-Sorrells/e9b8a8ebaa82ccb3fb21c9043993780c2c3012f3
[15] T. Pagliaroli, R. Camussi, P. Candeloro, O. Giannini, G. Bella, and R. Panciroli, Aeroacoustic Study of small scale Rotors for mini Drone Propulsion: Serrated Trailing Edge Effect. 2018. doi: 10.2514/6.2018-3449.
[16] P. Candeloro, R. E. Nargi, F. Patané, and T. Pagliaroli, "Experimental Analysis of Small-Scale Rotors with Serrated Trailing Edge for Quiet Drone Propulsion," J Phys Conf Ser, vol. 1589, 2020, Accessed: Feb. 16, 2023. [Online]. Available: https://www.semanticscholar.org/paper/Experimental-Analysis-of-Small-Scale-Rotors-with-Candeloro-Nargi/3abed7f78b5f87a79ba76c82fa31a6158a474737
[17] P. Candeloro, R. E. Nargi, E. Grande, D. Ragni, and T. Pagliaroli, "Experimental Fluid Dynamic Characterization of Serrated Rotors for Drone Propulsion," J Phys Conf Ser, vol. 1977, no. 1, p. 012007, 2021, doi: 10.1088/1742-6596/1977/1/012007.
[18] S. M. Hasheminejad, T. Chong, P. Joseph, and G. Lacagnina, Airfoil Self-Noise Reduction Using Fractal-Serrated Trailing Edge. 2018. doi: 10.2514/6.2018-3132.
[19] D. Ragni, F. Avallone, W. van der Velden, and D. Casalino, "Measurements of near-wall pressure fluctuations for trailing-edge serrations and slits," Exp Fluids, vol. 60, Nov. 2018, doi: 10.1007/s00348-018-2654-5.
[20] C. Arce León, R. Merino-Martínez, D. Ragni, F. Avallone, and M. Snellen, "Boundary layer characterization and acoustic measurements of flow-aligned trailing edge serrations," Exp Fluids, vol. 57, no. 12, p. 182, 2016, doi: 10.1007/s00348-016-2272-z.
[21] Y. Hong, D. Han, and K. Yee, "DESIGN PARAMETER STUDY OF DRONE BLADE CONSIDERING AEROACOUSTICS," in 31st Congress of the International Council of the Aeronautical Sciences, September 09-14, Belo Horizonte, 2018, pp. 1–8. Accessed: Nov. 03, 2022. [Online]. Available: https://icas.org/ICAS_ARCHIVE/ICAS2018/data/papers/ICAS2018_0216_paper.pdf
[22] Y. Wei, F. Xu, S. Bian, and D. Kong, "Noise Reduction of UAV Using Biomimetic Propellers with Varied Morphologies Leading-edge Serration," J Bionic Eng, vol. 17, no. 4, pp. 767–779, 2020, doi: 10.1007/s42235-020-0054-z.
[23] P. Chaitanya, S. Narayanan, J. Phillip, and K. Jae, "Leading edge serration geometries for significantly enhanced leading edge noise reductions," Apr. 2016. doi: 10.2514/6.2016-2736.
[24] P. Chaitanya et al., "Performance and mechanism of sinusoidal leading edge serrations for the reduction of turbulence–aerofoil interaction noise," J Fluid Mech, vol. 818, pp. 435–464, 2017, doi: DOI: 10.1017/jfm.2017.141.
[25] S. Narayanan, P. Chaitanya, S. Haeri, P. Joseph, J. W. Kim, and C. Polacsek, "Airfoil noise reductions through leading edge serrations," Physics of Fluids, vol. 27, no. 2, p. 025109, Feb. 2015, doi: 10.1063/1.4907798.
[26] P. Candeloro, D. Ragni, and T. Pagliaroli, "Small-Scale Rotor Aeroacoustics for Drone Propulsion: A Review of Noise Sources and Control Strategies," Fluids, vol. 7, no. 8, 2022, doi: 10.3390/fluids7080279.
[27] F. Moslem, M. Masdari, K. Fedir, and B. Moslem, "Experimental investigation into the aerodynamic and aeroacoustic performance of bioinspired small-scale propeller planforms," Proc Inst Mech Eng G J Aerosp Eng, vol. 237, pp. 75–90, 2022, Accessed: Feb. 18, 2023. [Online]. Available: https://www.semanticscholar.org/paper/Experimental-investigation-into-the-aerodynamic-and-Moslem-Masdari/c599c5138cbd00185eb90df00148b1fc08706fb7
[28] R. M. Ariefianto, R. N. Hasanah, Wijono, and R. A. Aprilianto, "Performance Investigation of a Humpback Whale-Inspired Vertical Axis Current Turbine," in Proceedings of the International Conference on Sustainable Environment, Agriculture and Tourism (ICOSEAT 2022), Atlantis Press, 2022, pp. 749–758. doi: 10.2991/978-94-6463-086-2_99.

DOI: ADD DOINUMBER HERE

[29] L. Wang, X. Liu, L. Wu, and D. Li, "Effect of the asymmetric bio-inspired trailing-edge serrations on sound suppression in a coupled owl-based airfoil," Applied Acoustics, vol. 191, p. 108667, 2022, doi: https://doi.org/10.1016/j.apacoust.2022.108667.
[30] I. Clark, W. J. Devenport, J. Jaworski, C. Daly, N. Peake, and S. A. Glegg, "The Noise Generating and Suppressing Characteristics of Bio-Inspired Rough Surfaces," in 20th AIAA/CEAS Aeroacoustics Conference, in AIAA AVIATION Forum. American Institute of Aeronautics and Astronautics, 2014. doi: doi:10.2514/6.2014-2911.
[31] I. A. Clark et al., "Bioinspired Trailing-Edge Noise Control," AIAA Journal, vol. 55, no. 3, pp. 740–754, Dec. 2016, doi: 10.2514/1.J055243.
[32] A. Afshari, M. Azarpeyvand, A. A. Dehghan, and M. Szőke, Trailing Edge Noise Reduction Using Novel Surface Treatments. 2016. doi: 10.2514/6.2016-2834.
[33] A. Afshari, M. Azarpeyvand, A. A. Dehghan, M. Szőke, and R. Maryami, "Trailing-edge flow manipulation using streamwise finlets," J Fluid Mech, vol. 870, pp. 617–650, 2019, Accessed: Feb. 18, 2023. [Online]. Available: https://www.semanticscholar.org/paper/Trailing-edge-flow-manipulation-using-streamwise-Afshari-Azarpeyvand/1759592d5202521d9fd84fae988801dada0299d6
[34] A. Bodling and A. Sharma, "Numerical investigation of noise reduction mechanisms in a bio-inspired airfoil," J Sound Vib, vol. 453, pp. 314–327, 2019, doi: https://doi.org/10.1016/j.jsv.2019.02.004.
[35] Y. Shi and S. Lee, "Numerical study of 3-D finlets using Reynolds-averaged Navier–Stokes computational fluid dynamics for trailing edge noise reduction," Int J Aeroacoust, vol. 19, no. 1–2, pp. 95–118, Mar. 2020, doi: 10.1177/1475472X20905053.
[36] F. Gstrein, N. Zang, and M. Azarpeyvand, "Application of Finlets for Trailing Edge Noise Reduction of a NACA 0012 Airfoil," in AIAA AVIATION 2020 FORUM, in AIAA AVIATION Forum. American Institute of Aeronautics and Astronautics, 2020. doi: doi:10.2514/6.2020-2502.
[37] F. Gstrein, B. Zang, Y. D. Mayer, and M. Azarpeyvand, "Airfoil Trailing-Edge Noise Reduction by Application of Finlets," AIAA Journal, vol. 60, no. 1, pp. 236–248, Sep. 2021, doi: 10.2514/1.J060699.
[38] S. Palani et al., Comparison of finlet rails and fences for trailing edge noise reduction in NACA0012 aerofoil. 2022. doi: 10.2514/6.2022-3015.
[39] V. B. Ananthan and R. A. D. Akkermans, "Trailing edge noise reduction using bio-inspired finlets," J Sound Vib, vol. 549, p. 117553, 2023, doi: https://doi.org/10.1016/j.jsv.2023.117553.
[40] "DJI-Phantom 3 DJI-9450 Rotor." Accessed: Jan. 05, 2023. [Online]. Available: https://grabcad.com/library/phantom-3-prop-1
[41] A. Zarri, E. Dell'Erba, W. Munters, and C. Schram, "Aeroacoustic installation effects in multi-rotorcraft: Numerical investigations of a small-size drone model," Aerosp Sci Technol, vol. 128, p. 107762, Sep. 2022, doi: 10.1016/J.AST.2022.107762.
[42] ANSYS, "Chapter 10: Modeling Flows with Moving Reference Frames," in ANSYS Fluent Users Guide , 2022, pp. 1661–1678.
[43] R. R. Mankbadi, S. O. Afari, and V. V Golubev, "High-Fidelity Simulations of Noise Generation in a Propeller-Driven Unmanned Aerial Vehicle," AIAA Journal, vol. 59, no. 3, pp. 1020–1039, Dec. 2020, doi: 10.2514/1.J059117.
[44] TCAE, "Acoustic Benchmark Propeller DJI-9450." Accessed: Dec. 10, 2022. [Online]. Available: https://www.cfdsupport.com/acoustic-benchmark-propeller-dji-9450.html
[45] C. Russell, J. Jung, G. Willink, and B. Glasner, "Wind Tunnel and Hover Performance Test Results for Multicopter UAS Vehicles," in American Helicopter Society (AHS) International Annual Forum and Technology Display, May 2016, pp. 1–20. Accessed: Oct. 17, 2022. [Online]. Available: https://ntrs.nasa.gov/citations/20160007399
[46] C. S. Thurman, N. S. Zawodny, and J. S. Baeder, "Computational Prediction of Broadband Noise from a Representative Unmanned Aerial System Rotor," in 76th Annual Forum & Technology Display, Virginia Beach, VA, Jun. 2020, pp. 1–9. Accessed: Apr. 23, 2023. [Online]. Available: https://ntrs.nasa.gov/citations/20205003566
[47] ANSYS, "Chapter 19: Predicting Aerodynamically Generated Noise," in ANSYS Fluent Users Guide , 2022, pp. 2417–2465.
[48] S. O. Afari and R. R. Mankbadi, "Simulations of multi-rotor interaction noise at hovering & forward flight conditions," Int J Aeroacoust, vol. 0, no. 0, p. 1475472X231152608, Jan. 2023, doi: 10.1177/1475472X231152608.
[49] L. Lopes, D. Jr, D. Nark, and K. Wiedemann, Identification of Spurious Signals from Permeable Ffowcs Williams and Hawkings Surfaces. 2017.